Sensors and Actuators A 263 (2017) 600–609

Contents lists available at ScienceDirect

Sensors and Actuators A: Physical

journal homepage: www.elsevier.com/locate/sna

Seesaw-structured triboelectric nanogenerator for scavenging electrical energy from rotational motion of mechanical systems

Jingui Qian [a], Xuan Wu [a,b], Dong-Su Kim [a], Dong-Weon Lee [a,*]

[a] MEMS and Nanotechnology Laboratory, School of Mechanical Engineering, Chonnam National University, Gwangju 61186, Republic of Korea
[b] School of Mechanical Engineering, JiangSu University, Zhenjiang 212013, China

ARTICLE INFO

Article history:
Received 15 March 2017
Received in revised form 5 July 2017
Accepted 10 July 2017
Available online 17 July 2017

Keywords:
Triboelectric nanogenerator
Seesaw structure
Contact mechanism
Magnetically coupled
Rotational motion

ABSTRACT

This study reports a seesaw-structured triboelectric nanogenerator (S-TENG) for efficiently harvesting electrical energy from rotational motion of mechanical systems. The designed S-TENG with two arms is comprised four contact-pair units with distinctly different triboelectric polarity materials. The generated electric power from the unique structure based on the seesaw system was double at every machine rotation cycle. A magnetically coupled contact mechanism was also utilized to reduce the wear of the polymer material. It was experimentally confirmed that the proposed design significantly improved the reliability and long-term stability in comparison with currently available TENG systems based on the sliding mechanism. In addition, micro-pyramid patterns were formed on the polymer surface to enhance the surface charge density. Through systematic experiments with a variety of operational conditions, an instantaneous maximum output power density of 13.86 W/m^2 was achieved at a rotation speed of 200 rpm under a constant magnetic field strength of 0.2 T. The S-TENG has been demonstrated as a direct power source to drive small electronic devices such as commercial LED arrays and to charge an energy storage unit. This study further expanded the potential applications of the S-TENG to realize the self-powered wireless sensor nodes such as structural health and condition monitoring system.

1. Introduction

Over the past half century, the development of wireless sensor networks (WSNs) has been considered as one of the most significant technologies in the field of information transmission [1–3]. However, the highlighted bottleneck for developing WSNs is to afford a long-term power supply system, because the limited power of commercial batteries leads to issues of frequent replacement and inconvenient installation [4,5]. Therefore, harvesting electrical energy from the ambient environment by an effective and sustainable method is highly desirable [6–8]. Among multiple energy sources, mechanical energy harvesting has attracted extensive interest because of its many advantages, including no restrictions of time, climate, or location, plentiful renewability, and universal availability. The emerging technologies for scavenging mechanical energy have been extensively developed based on piezoelectric [9–12], electromagnetic [13–16], and electrostatic [17,18] principles. However, the low output power of the energy harvesters based on aforesaid principle cannot meet the required values of the electrical energy for most of the wireless sensors. Recently, a cost-effective and robust triboelectric nanogenerator (TENG) [19–21] was introduced for scavenging electrical energy from mechanical energy based on the triboelectric effect coupled with electrical induction [22,23], which can generate much higher output power than the available energy harvester based on piezoelectric, electromagnetic, and electrostatic principles (Support information S1). Among various TENGs, the rotational TENG can be utilized to harvest rotating mechanical energy through a periodic in-plane sliding model between two materials with different triboelectric polarities. For instance, Bai et al. [24] demonstrated a cylindrical rotating triboelectric nanogenerator based on sliding electrification for harvesting mechanical energy from rotational motions. Lin et al. [25] introduced a disk triboelectric nanogenerator with segmental structures for harvesting rotational mechanical energy. Zhang et al. [26] reported a single-electrode-based rotating triboelectric nanogenerator for harvesting energy from tires. Lia et al. [27] proposed a single-electrode-based rotational triboelectric nanogenerator formed by two wheels and a belt as a self-powered contact area and an eccentric angle sensor. However, these kinds of rotational TENGs with sliding mechanisms have drawbacks in long-term use and persistent high energy conversion efficiency. For example, the assembly configuration of currently available

* Corresponding author.
E-mail address: mems@jnu.ac.kr (D.-W. Lee).

http://dx.doi.org/10.1016/j.sna.2017.07.021
0924-4247/

TENGs in rotating systems [24–30] leech on to external mechanical motion, which leads to restrictions and inconvenience on more application scenarios [31]. The sliding mechanism of TENGs quickly damages the polymer surface morphology as a function of working time [32,33] and substantially decreases the device reliability and life [34]. As well, higher temperature can result when a TENG works at a high rotation speed or after a long-term friction process, which has been proved to largely influence the energy conversion efficiency [35].

In this study, we introduce a durable and high-performance seesaw-structured triboelectric nanogenerator (S-TENG) combined with the rotating machineries. The driving force for the seesaw structure is generated by a magnetic coupling between the TENG and the rotational motion. The S-TENG was designed with distinctly different triboelectric polarity materials based on the contact mechanism. A polymer substrate with a micro-pyramid pattern enhanced the charge accumulation on the surface. Two movable seesaw-structured electrodes were employed to quadruple the contact area and produce double the electrical energy of each rotation cycle. An important aspect of introducing the magnetically coupled contact mechanism was to reduce the wear caused by currently available TENGs based on sliding mechanisms. The proposed design significantly increased the reliability and long-term stability of the TENGs applied in machines with a rotating part. The fabricated S-TENG was successfully employed as a direct power source to illuminate a large number of LEDs and to accumulate electrical energy in a capacitor.

2. Material and methods

2.1. Fabrication of micro-pyramid PDMS film

After a standard cleaning, a 4-in Si wafer (Fig. S2a) was placed in a furnace to form a 300-nm-thick silicon dioxide (SiO_2) layer on the surfaces (Fig. S2b). Next, a positive photoresist was coated on the wafer and patterned to make an array of squares (Figs. S2c, d). The SiO_2 layer was selectively etched using a buffered HF solution, and the silicon substrate was anisotopically wet-etched with the patterned SiO_2 layer (Fig. S2e). After removing the photoresist using an acetone solution, the SiO_2 mask layer was completely removed using the buffered HF solution (Fig. S2f). The Si wafer with reverse micro-pyramid structures was used as a master to duplicate the structures on the PDMS (polydimethylsiloxane) thin film. In general, the Si mold was quite hydrophilic, and thus the PDMS had a good affinity to the Si surface. This adhesion force was strong enough to make peeling impossible. To reduce the adhesion force between the Si matter and the PDMS film, the prepared Si master mold was cleaned with acetone and isopropanol, and the surface was then treated with a trimethylchlorosilane solution (Sigma-Aldrich) to change the surface condition from hydrophilic to hydrophobic. To fabricate the PDMS thin films with micro-pyramid patterns, a PDMS elastomer and cross-linker were mixed (base: curing agent = 10:1) and then spin-coated on the Si master molds. After a degassing process of more than 30 min in a vacuum chamber, the spin-coated PDMS was cured at 70 °C for 4 h (Fig. S2g). The cured PDMS thin film with a micro-pyramid surface was then drawn off from the Si mold (Fig. S2h).

2.2. Fabrication of S-TENG device

The S-TENG (measuring 88 mm × 44 mm × 34.8 mm) had a seesaw structure and an outer frame. The seesaw body and outer frame (Fig. S3a1, b1) was fabricated using a 3-D printer (3-D System, Corp, Rock Hill, USA). Two NdFeB magnets (20 mm in diameter and 3 mm thick) were placed on both wings of the seesaw structures (Fig. S3a2) and covered with square plates (Fig. S3a3). Four rubber sponges of 2-mm-thick were bonded to the seesaw (Fig. S3a4) and a 60-μm-thick aluminum film employed as triboelectric friction electrodes was coated on each sponge (Fig. S3a5). As shown in Fig. S3b2, four rubber sponges were employed to ensure the long-term stability of the TENG electrodes. The sponges were coated with a 60-μm-thick copper film (Fig. S3b3), and then an 800-μm-thick PDMS film with surface micro-pyramids (Fig. S3b4) was bonded to the copper film. After assembling a rotating shaft (Fig. S3b5), the fabricated seesaw structure was combined with the outer body (Fig. S3a6, b6) and manually packaged as shown in Fig. S3b7. An optical image of the fabricated S-TENG is shown in Fig. S3b8. The total area of contact for the generation of triboelectric energy was about 48 cm^2.

2.3. Electrical measurement system and experiment setup

A BLDC geared motor (BL5057, D&J WITH Co., Ltd., South Korea) and its driver (FTBL-V1) were employed to create rotational motion at various operation speeds. The DC supply for the motor and its driver was an Agilent E3642A power supply (Agilent Technologies, Inc, USA). A LZ-643 G meter (Linkjion Technology Co., Ltd., Hunan, China) was used to measure the magnetic field strength. A Tektronix TDS 2014 B Oscilloscope (Tektronix, Inc, USA) and an SR-570 low-noise current amplifier (Stanford Research System) were used to measure the open-circuit voltage and short-circuit current. Periodic contact and separation between two triboelectric friction layers were generated by a non-contact magnetic force. A higher DC motor speed was desirable to increase the amount of contact; however, this also reduced the magnetic coupling effect, which influenced the amplitude of the output voltage. A commercial wireless temperature sensor (eZ430-RF2500, Texas Instruments) was employed to demonstrate the feasibility of S-TENG for real applications.

3. Results and discussion

A schematic view of the designed S-TENG is illustrated in Fig. 1a. As shown in Fig. 1b, the S-TENG was positioned on the top of two circular disks at a certain distance. The circular disks had a permanent magnet on the side plane of each disk. The rotation speed of the circular disk was controlled by the DC motor. The rotating magnets on the disk provided a non-contact magnetic force to other permanent magnets placed on the wings of the seesaw structure. Therefore, a periodic clockwise and anticlockwise rotational motion of the seesaw structure was achieved because of the magnetic-coupling force from the rotational system. Here, the seesaw structure and outer frame were manufactured using an acrylic material because of its excellent properties, such as light weight, good machinability, and proper strength. The high-density sponges attached to both sides of the seesaw provided a good shock-resistant buffer layer, resilience, and elasticity and guaranteed the robustness and tolerance of the seesaw structure at high rotation speeds. The aluminum thin film attached to the surface of the sponges played the dual role of a positive triboelectric friction material and an inductive electrode. Four oblique planes were formed on the inner side of the acrylic frame, and the same sponges in the shape of a square plate were adhered to the four oblique planes. On the top surface of the sponges, a layer of copper film followed by a layer of the polymer film was conformably attached. The copper film served as the back electrode of the S-TENG. A PDMS film was chosen as the polymer film because of its intense negative triboelectric polarities. The surface morphology of the PDMS film was modified as a micro-structure pattern to strengthen the charge transfer. The SEM (scanning electron microscope) image of the PDMS surface is shown

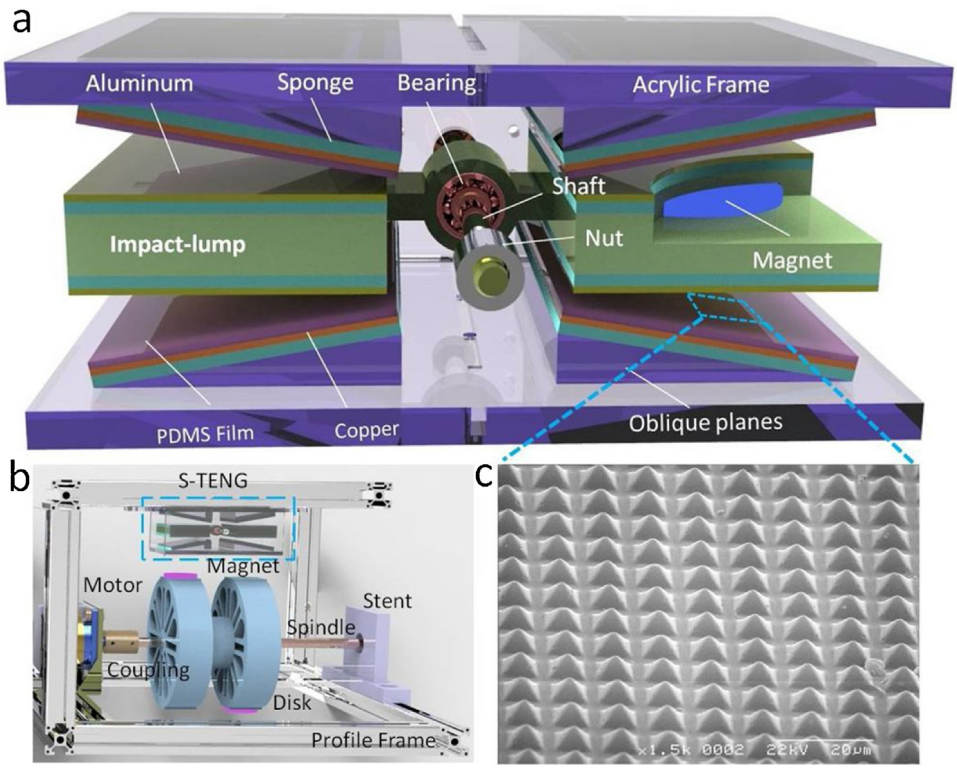

Fig. 1. (a) Schematic illustration showing the structural design of the S-TENG. (b) Schematic of the S-TENG rotating system setup. (c) SEM image of PDMS film surface with a micro-pyramid array pattern.

in Fig. 1c. The micro-pyramid arrays with an average side length of 6 μm was formed by using conventional MEMS technologies such as photolithography, anisotropic silicon etching, PDMS casting etc. (Support information S2) [36,37]. The unique structural design of the seesaw system can increase the contact area by four times and generate twice the electric output signal at every machine rotation cycle. As for the rotation system, a speed-control motor and its driver were mounted on an aluminum profile frame that was utilized to drive the rotating motion at various speeds. One end of the spindle was fixed to a stent, and the other end was connected to the motor by a coupling element. Two disks with permanent magnets were positioned at the middle of the spindle. In addition, the S-TENG was positioned on an aluminum profile frame based on a noncontact configuration for harvesting rotational energy. The magnetic field strength was determined by changing the gap between the rotating magnets and the wings of S-TENG device. The operation of the S-TENG is demonstrated in Video S1.

The working principle of a triboelectric nanogenerator can be explained on the basis of the contact electrification coupling with electrostatic induction [38]. Here, the process of electricity generation of four individual contact-pair units is illustrated in Fig. 2a. At State I, the aluminum film maintains full contact with the PDMS surface. A charge transfer occurs upon contact between two triboelectric friction layers. Owing to the opposite triboelectric polarities, the negative electrons from the aluminum film are transferred onto the surface of the PDMS thin film. Since the surfaces of the two triboelectric friction layers make complete contact, these two opposite polarity charges are balanced out, and no electron flow occurs in the external circuit. Once a relative distance is caused as a result of rotation of the seesaw structure, the triboelectric charges on the two discontiguous surfaces cannot be compensated. The negative electrodes on the PDMS film drive free electrons on the back copper electrode to the aluminum electrode through the external circuit because of electrostatic induction, which is trying to neutralize the positive triboelectric charges on the aluminum electrode and to leave the positive induced charges behind on the back electrode (State II). The induced electron flow lasts until the distance between the two discontiguous surfaces reaches the maximum and the positive triboelectric charges are fully screened by induced electrons (State III). As the relative anticlockwise rotation continues, the PDMS film comes into contact with the aluminum electrode (State IV) and the induced electrons flow back in the opposite direction until the fully aligned position is restored (State I). Therefore, AC electricity is generated in each cycle of the electricity generation process.

To acquire a more quantitative understanding of the operation principle, a numerical simulation via the finite element method was employed to calculate the potential distribution of the two electrodes in an open-circuit condition [39]. The model had the same dimensions as the real device. The triboelectric charge density on the aluminum and PDMS layer surface was $\pm 10\ \mu C/m^2$ [40]. Fig. 2b shows the calculated potential distribution on the inductive electrodes during the continuous movement of the seesaw structure from State I to State IV. Peripheral region A had a cuboid-shaped geometry to assume the entire simulation physics field that was filled with air with a relative permittivity of 1.0006. The bottom side of the cuboid-shaped geometry was used as a reference in the simulation and was grounded. In Stage I, the two triboelectric friction layers were in full contact with each other, and the electric potential difference between the PDMS and aluminum thin layers maintained a minimum value of 1.09 kV. Subsequently, with the clockwise rotation of the seesaw, the electric potential difference between the two layers increased by 8.85 kV as the seesaw maintained a state of balance (Stage II) and attained the peak value of 9.23 kV when the separation completed (Stage III). When the seesaw structure reached a second balance state (Stage IV), the electric potential difference decreased as the distance between the two layers began to contract and exhibited the same behavior as in Stage

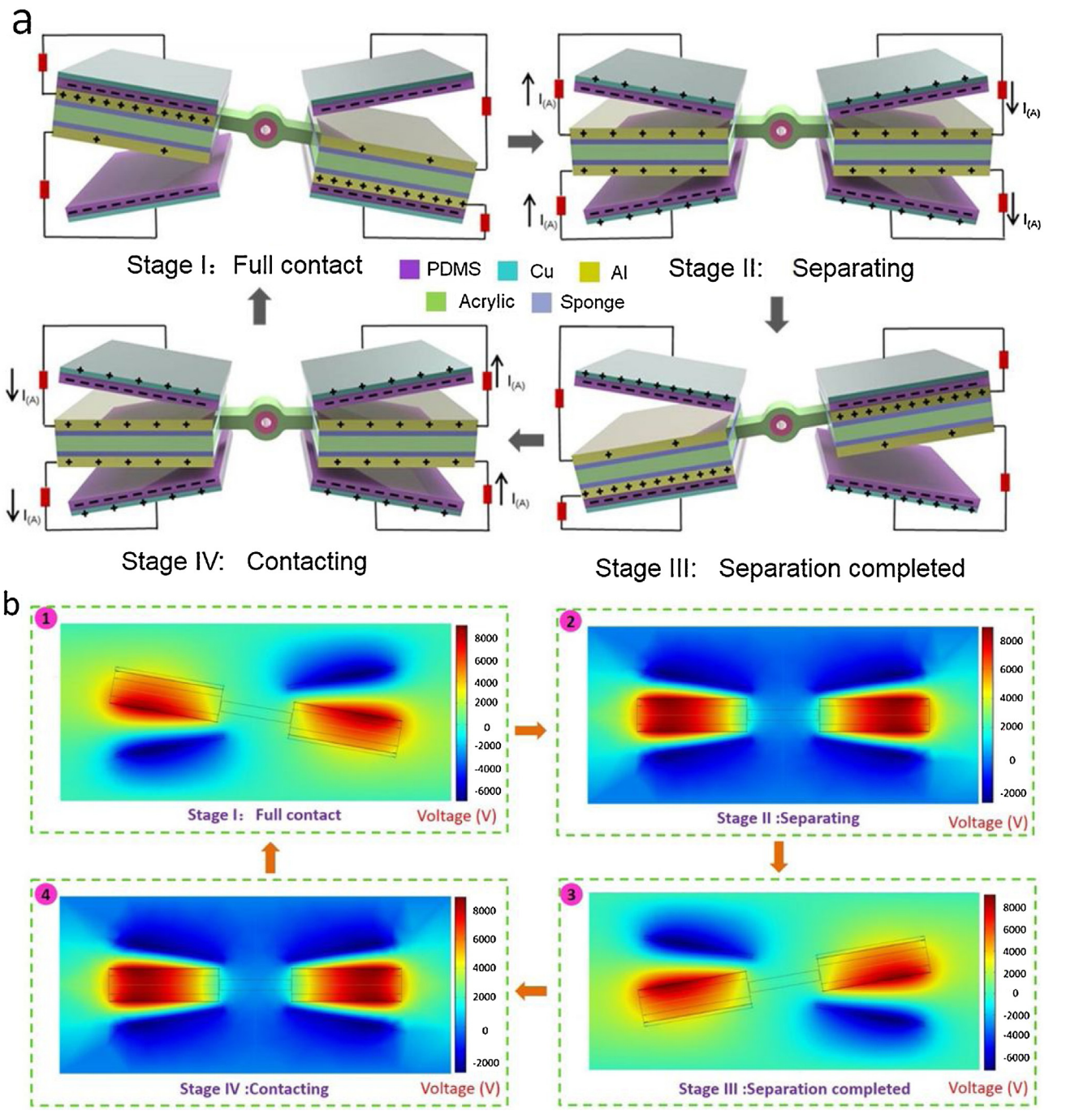

Fig. 2. (a) Schematic illustrations showing the working principle of the proposed S-TENG with electron flow diagrams of four consecutive stages within a full cycle of electricity generation. (Note that four contact-pair units are shown with surface charges for clarity of illustration, and other components of the S-TENG device are hidden for easier presentation.) (b) Calculated potential distribution on the inductive electrodes via the finite element method. The model had the same structure and dimensions as the real device. The triboelectric charge density was about 10 $\mu C/m^{-2}$.

II. As can be seen from the simulation results, the electric potential difference between the PDMS and the aluminum layers increased as the separation between the two layers increased, resulting in a flow of electrodes from the copper electrodes to the aluminum electrodes.

The S-TENG had a special structure including four individual contact-pair units based on a nonparallel charge separation mechanism. The triboelectric contact pairs of the TENGs of the nonparallel contact-mode were mainly derived from two categories, including two types of dielectric-to-dielectric and conductor-to-dielectric. First, to thoroughly investigate the intrinsic output characteristics, the theoretical model [41,42] of the S-TENG employed in the conductor-to-dielectric nonparallel-plate contact mode was built as depicted in Fig. 3. The open-circuit voltage and the short-circuit current generated across the output terminal can be defined by

$$V_{oc} = \frac{\sigma S\theta(t)}{\varepsilon_0 l In(R_1/R_2)}, \quad (1)$$

$$I_{sc} = \frac{C^2 \sigma d_0 w(t)}{In(R_1/R_2) l \varepsilon_0{}^2}, \quad (2)$$

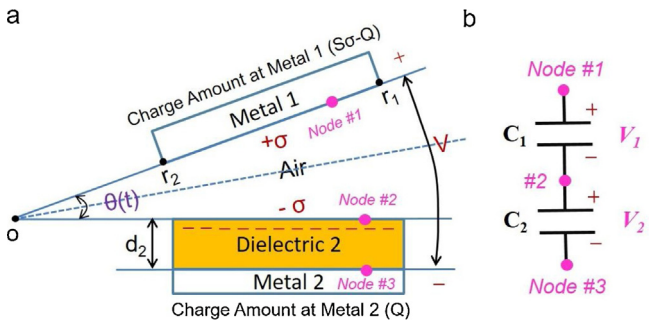

Fig. 3. (a) Theoretical models for conductor-to-dielectric nonparallel-plate contact mechanism TENG. (b) Equivalent circuit diagram of theoretical models.

Where is calculated by

$$C = \frac{\varepsilon_0 S}{d_0 + \frac{\theta(t)S}{l} In\frac{R_2}{R_1}}, \quad (3)$$

$$d_0 = \frac{d_2}{\varepsilon_2}, \quad (4)$$

In these equations, ε_0 is the vacuum permittivity, s is the contact area, σ is the generated surface triboelectric charge density, $w(t)$ is the rotational angle velocity at a given state, $\theta(t)$ is the relative angle between the metal and dielectric, ε_2 and d_2 represent the relative permittivity and thickness of the dielectric, R_1 is the line length between the point o and point r_1, R_2 is the line length between the point o and point r_2, respectively. These formulas indicate that the only influencing factor of the open-circuit voltage (V_{oc}) is the generated triboelectric charge density, but both the contact speed and the generated triboelectric charge density were directly proportional to the short-circuit current (I_{sc}). The theoretical model of the TENGs employed in the dielectric-to-dielectric nonparallel-plate contact mode and the specific details for calculation procedures are described in supporting information S4.

To investigate the electrical output performance, various short-circuit current and open-circuit voltage curves of the S-TENG were measured using the experimental setup. First, the output characterization of the S-TENGs with two different PDMS surface features were evaluated and compared to understand the importance of surface morphology in power generation. Under a magnetic field strength of 0.2 T, the output V_{oc} curves were measured using flat and micro-pyramid-patterned PDMS films at a rotation speed of

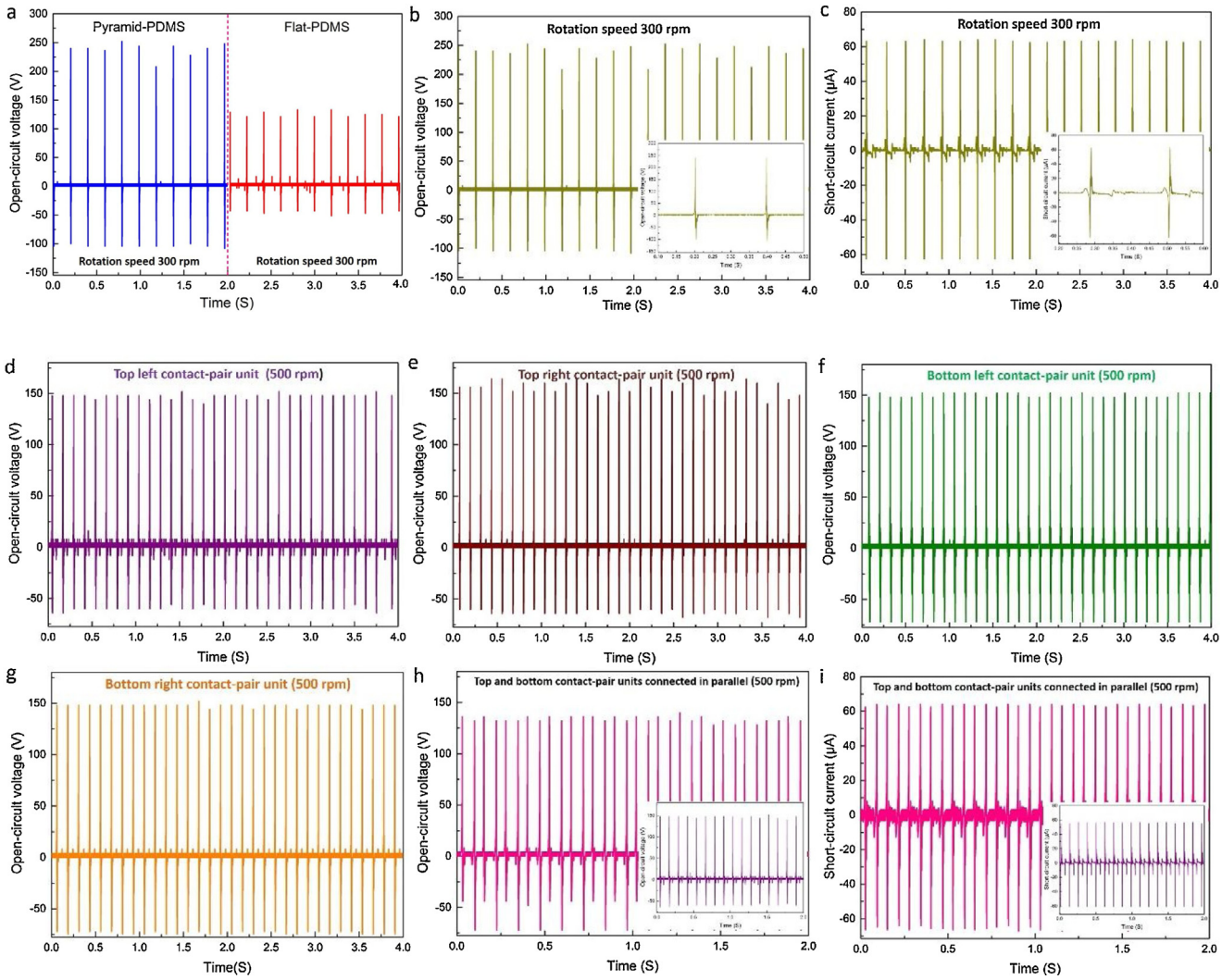

Fig. 4. Electrical output of the S-TENG under a magnetic field strength of 0.2 T. (a) Measured output V_{oc} curves using flat PDMS thin film and micro-pyramid pattern at a rotation speed of 300 rpm. (b) and (c) Measured V_{oc} and I_{sc} curves at a rotation speed of 300 rpm, respectively (inset: enlarged view of voltage and current peaks). (d–g) Measured V_{oc} curves of four different contact pairs at a rotation speed of 500 rpm. (h and i) Measured V_{oc} and I_{sc} curves with two contact pairs (top and bottom) connected in parallel at a rotation speed of 500 rpm.

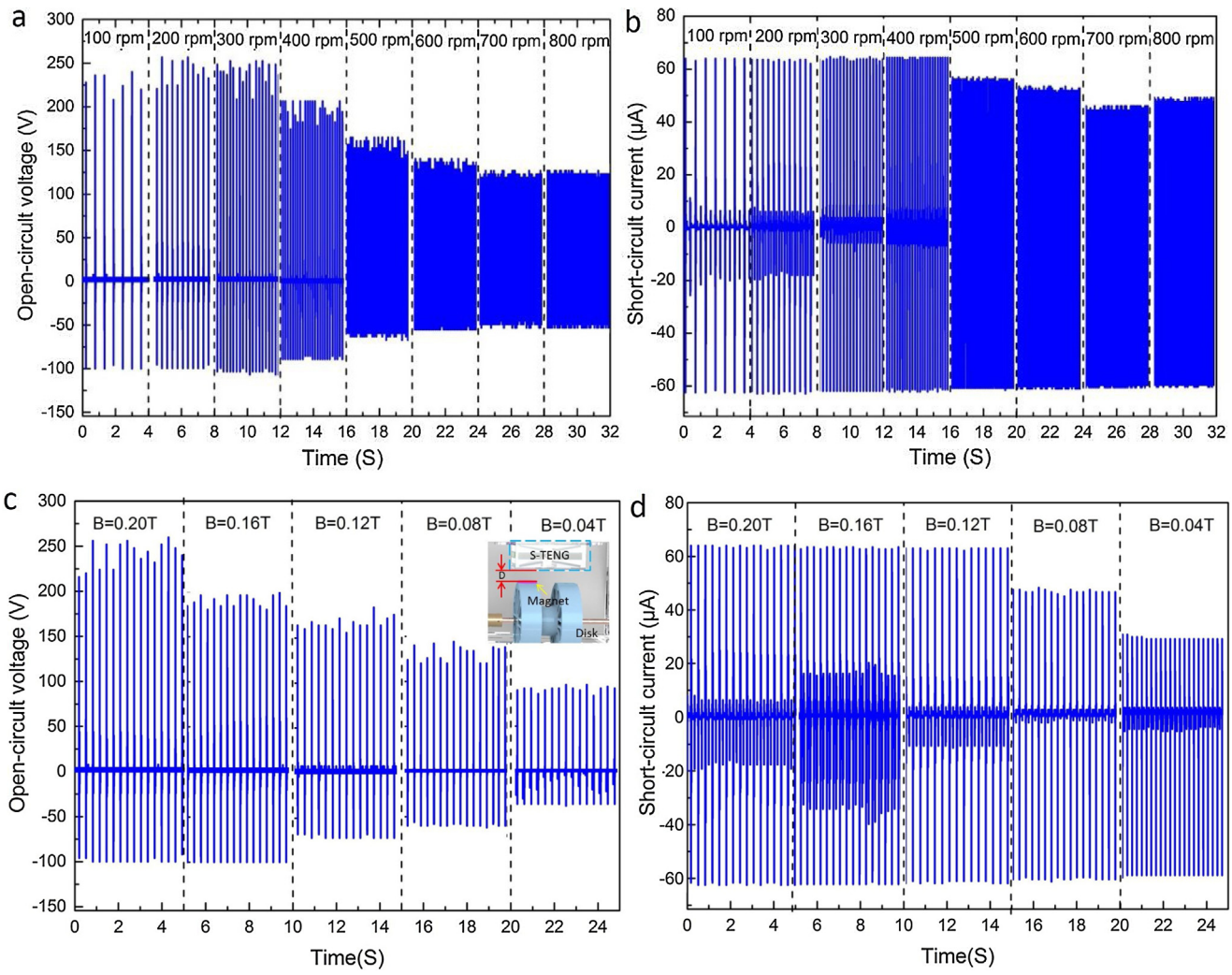

Fig. 5. Electrical output performance of the S-TENG (note that the electrical output of only one contact pair is shown for easily presentation). (a) Measured V_{oc} curves with rotation speeds from 100 to 800 rpm under a magnetic field strength of 0.2 T. (b) Measured I_{sc} curves with rotation speeds from 100 to 800 rpm under a magnetic field strength of 0.2 T. (c) Measured V_{oc} curves under magnetic field strengths from 0.04 T to 0.2 T with a rotation speed of 200 rpm. (d) Measured I_{sc} curves under magnetic field strengths from 0.04 T to 0.2 T with a rotation speed of 200 rpm.

300 rpm as shown in Fig. 4a. This result clearly indicates that the output efficiency of the pyramid-type surface was much better than that of the flat PDMS surface because of the higher charge density at the top of the pyramid which increased the contact area during the periodic contact process. The electrical output (V_{oc} and I_{sc} curves) of the S-TENG with the pyramid-type PDMS at a rotation speed of 300 rpm are presented in Fig. 4b and c. The inset is an enlarged view of the voltage and current peaks exhibiting continuous AC output and oscillating behavior between zero and the peak value. The maximum output of V_{oc} and I_{sc} were as high as 260 V and 64 μA (corresponding to a power density of 13.86 W/m^2). Fig. 4d–g show the equivalent and stable output V_{oc} behaviors of four different contact pairs in the left and right sides at a rotation speed of 500 rpm. As shown in Fig. 4h–i, the number of peaks in V_{oc} and I_{sc} doubled when two contact pairs (top and bottom) were connected in parallel by an electrical wire. The insets show the output V_{oc} and I_{sc} curves from one of the four contact pairs. These results indicate that the fabricated S-TENG device with four contact-pair units had a high-performance because of its increased contact area.

To investigate the influence of the rotational speed and magnetic field strength on the output performance of the S-TENG, additional experiments were conducted with the fabricated S-TENG as shown in Fig. 5. Fig. 5a and b show the measured V_{oc} and I_{sc} characteristics at rotation speeds from 100 to 800 rpm under a magnetic field strength of 0.2 T. Fig. 5c and d show the measured V_{oc} and I_{sc} characteristics under magnetic field strengths from 0.04 T to 0.2 T at a constant rotational speed of 200 rpm. These results indicate that the outputs V_{oc} and I_{sc} of the S-TENG increased with an increase in the magnetic field strength from 0.04 T to 0.2 T. However, V_{oc} and I_{sc} decreased with an increase in the rotation rate from 100 to 800 rpm. These results indicate that the strength of the magnetic field affects the contact force during the triboelectricfriction material contact. Increased contact force has a linear relationship with polymer surface deformation and increases the contact area. Increasing the contact charging area of the S-TENG leads to a larger triboelectric potential and increment of triboelectric charge density between the polymer surface and the electrodes, leading to a higher induced charge transfer [43]. Referring to study [44,45], a linear relationship between velocity and output current can be attributed to the increasing frequency [24]. Considering the structure and operation principle of the available TENG, changing the linear rotational rate had no influence on the transferred charge density under a constant applied force, and a higher linear rotational rate resulted in a faster charge transfer rate. In addition, the V_{oc} maintained a stable trend at different rotation rates because the voltage was only a function of distance. However, when the

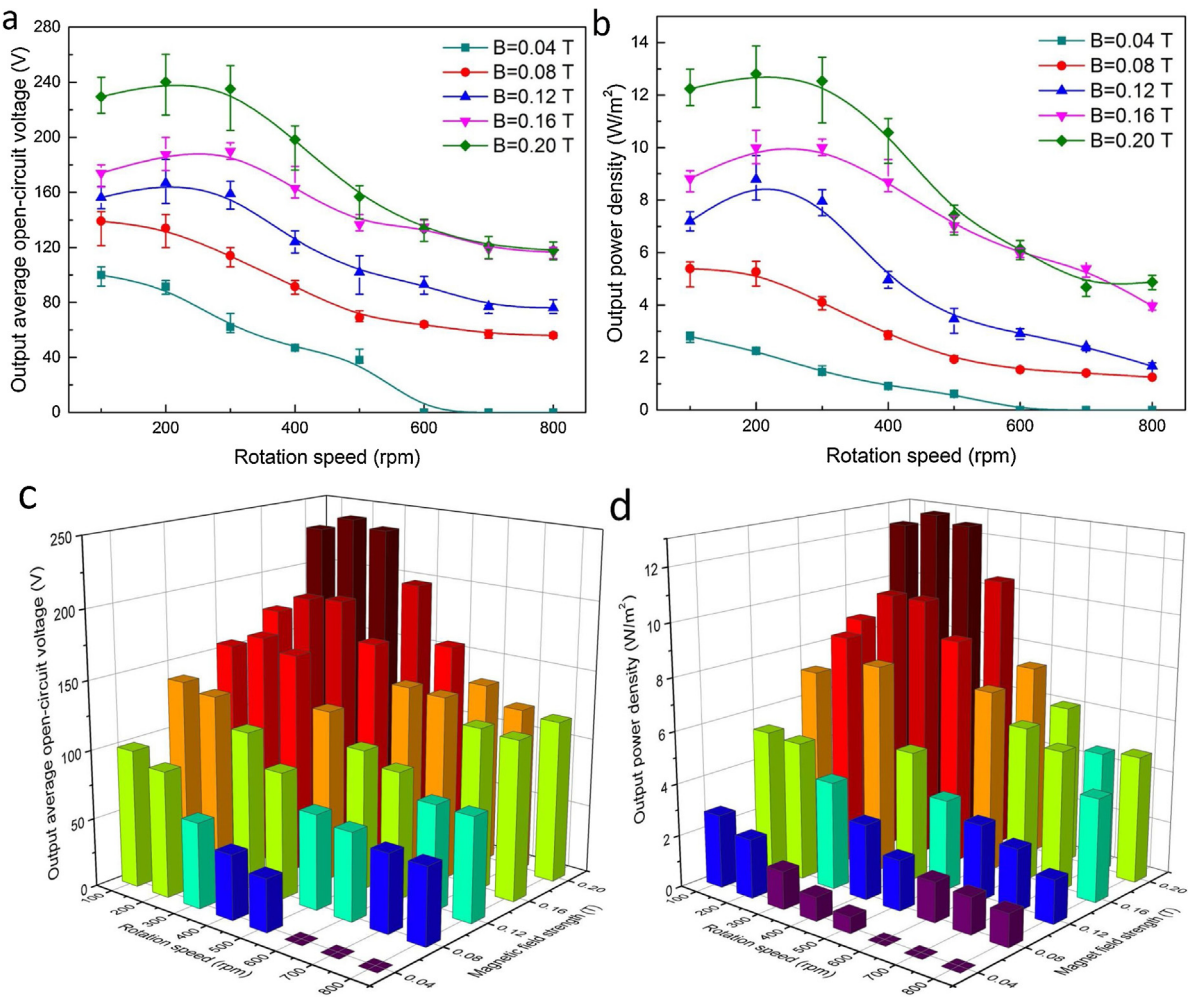

Fig. 6. Influence of rotation speed and magnetic field strength on output performance of the S-TENG. (a) Graph of output V_{oc} at various rotation rates. (b) Graph of output power density at various rotation rates. (c) 3D surface graph of average output open-circuit voltage vs. rotation speed and magnetic field strength. (d) 3D surface graph of output power density vs. rotation speed and magnetic field strength.

S-TENG scavenges mechanical energy from the rotating motion, according to the dynamic analysis and magnetic simulation of the entire rotation period (Support information S5 and Video S2), the linear rotation rate nonlinearly influenced the contact force between the aluminum and the PDMS triboelectric layer, and the contact force was reduced constantly with an increased rotation rate. Therefore, the output power slightly decreased. However, it would be possible to compensate the depressed output power by increasing the magnetic field strength. Further experiments were performed to systematically explore the influence of the rotation speed and magnetic field strength on the output characterization as shown in Fig. 6a and b. The average output open-circuit voltage and power density decreased with an increase in the rotation speed. The average open-circuit voltage and power density as a function of magnetic field strength and rotation speed are plotted in Fig. 6c and d. These results indicate that the electrical output can be effectively collected in wide ranges of rotation speed and magnetic field strength with the fabricated S-TENG device. Higher output can be achieved if stronger magnets are employed or lower rotational velocity is applied.

It is very important to characterize the internal impedance characteristics of the fabricated S-TENG to be able to decide the value of the load resistor for maximum power transfer. In this respect, the electric output performance of the S-TENG was systematically studied with different load resistances under a magnetic strength of 0.2 T. Fig. 7a shows the resistance dependence on output voltage and current from 1 kΩ to 1 GΩ at a rotation speed of 500 rpm with only one contact-pair unit. The output current decreased with increasing resistance, while the output voltage exhibited the reverse trend, but both the current and voltage tended to saturate at both high and low values of resistance. The internal impedance value of the S-TENG was also experimentally confirmed with short-circuit and open-circuit configurations. The power densities corresponding to the values of an external resistor are plotted in Fig. 7b. The maximum power from one section of the S-TENG was about 2.6 W/m^2 at 1 MΩ. This value is high enough to operate most small wireless sensor units. When the S-TENG is connected with a diode bridge for rectification (insert in Fig. 7d, the electric circuit diagram of capacitor charge), the induced charges can be accumulated into a capacitor. As illustrated in Fig. 7c, a 10-μF capacitor was charged by S-TENGs with different numbers of contact-pair units at a rotation speed of 500 rpm. An enhancement on equivalent DC output voltage from 3.4 V to 14.2 V was achieved by increasing the number of contact-pair units from one to four. To demonstrate the ability of the fabricated S-TENG to serve as a direct power source for small electronic devices, a total of 120 commercial LEDs divided into two arrays were connected to four contact-pair units as external loads. The LED connection schematic is illustrated in Fig. 7e. The output power generated by the periodic clockwise and anticlockwise rotational motion of the S-TENG seesaw structure was about

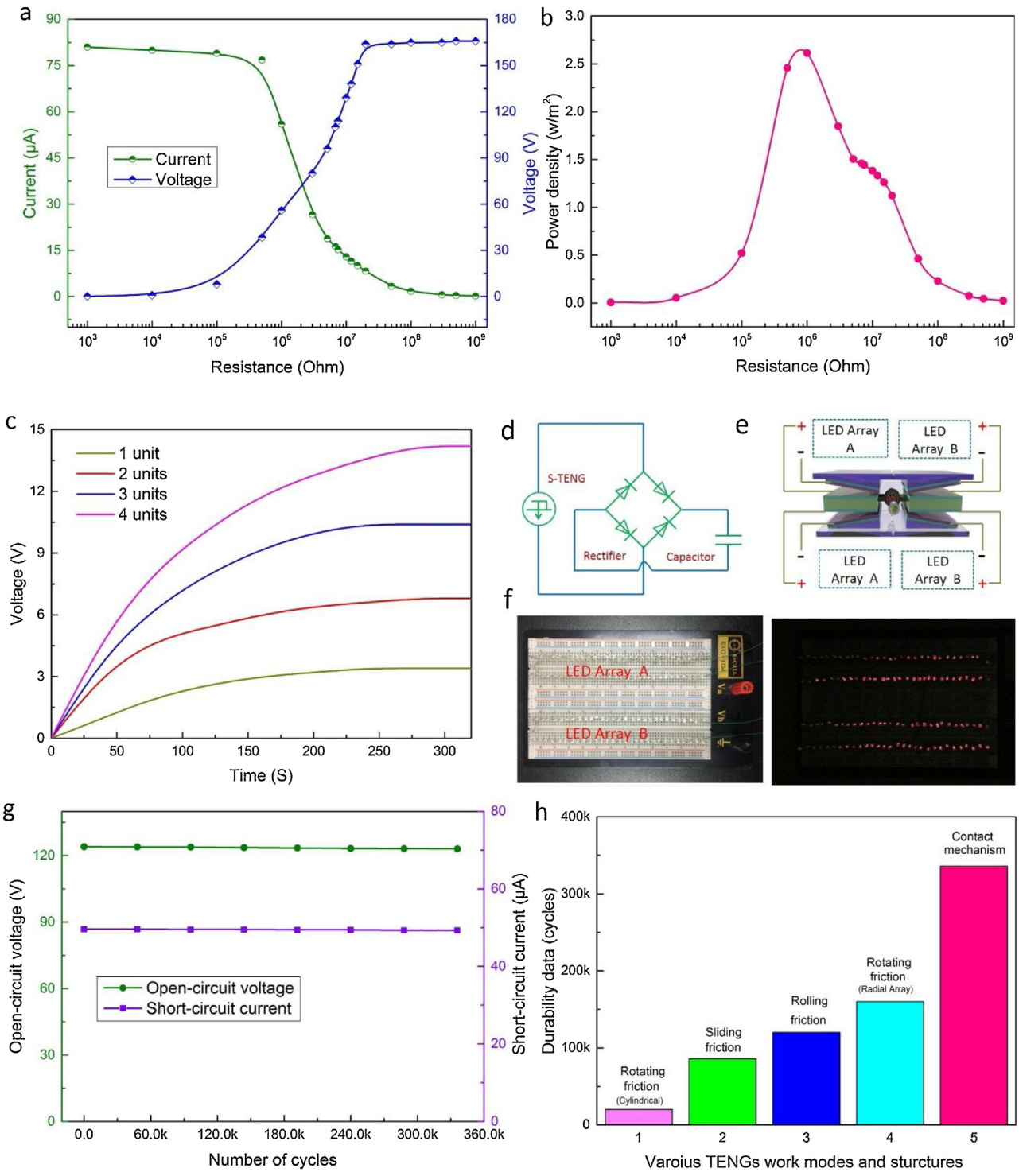

Fig. 7. Output performance of the S-TENG. (a) Relationship between output voltage/current and resistance of external load at 500 rpm. (b) Relationship between effective power density and resistance of external load at 500 rpm. The maximum power density was received when the external resistance was 1 MΩ. (c) Measured voltage of a 10-μF capacitor charged by the S-TENG with different numbers of contact-pair units at a rotation speed of 500 rpm. (d) Capacitor charging circuit diagram. (e) Schematic of S-TENG connected to four LED arrays. (f) Demonstration of the S-TENG as a direct power source for driving 120 LEDs when the LEDs were on. (g) Robustness of the S-TENG at a rotation speed of 800 rpm. The electric output remained stable, but a slight decline of the maximum V_{oc} and I_{sc} occurred. (h) Durability data of the S-TENG compared to TENGs with various work modes and device structures.

7.43 W/m^2 at a rotation rate of 500 rpm. As shown in Fig. 7f, the 120 LEDs were energized alternately by two diagonally placed contact-pair units of the S-TENG (see Video S3). The robustness of the S-TENG was also examined by repeated contacts at a rotation speed of 800 rpm. As shown in Fig. 7g, a slight decrease of 0.6% (from 49.6 to 49.3 μA) was observed for the I_{sc}, while the V_{oc} dropped slightly from 124 to 123 V (~0.8%). These results demonstrated the prominent durability of the S-TENG based on the contact mechanism, which were considerably better than that of other TENGs based on sliding mechanisms including rotating friction, rolling friction, and sliding friction [24,34,46,47]. Therefore, the S-TENG has a substan-

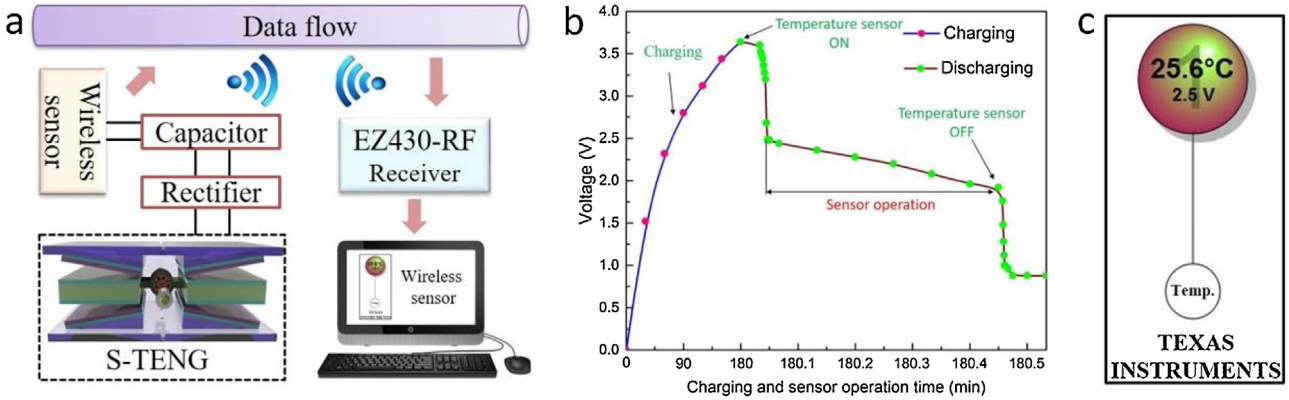

Fig. 8. Demonstration of a wireless temperature sensor powered by the S-TENG. (a) A schematic diagram of the wireless temperature sensor systems. (b) Charging and discharging behaviors of a 3 mF capacitor employed as a power source. (c) Temperature information displayed on a monitor. The temperature data is transmitted from the wireless sensor to the computer.

tially increased service life compared to that of conventional TENGs for rotational energy harvesting as shown in Fig. 7h.

A wireless temperature monitoring sensor system (eZ430-RF2500, Texas Instruments) was employed to demonstrate the feasibility of the proposed S-TENG. Fig. 8a shows schematic diagram of the wireless sensor node combined with the S-TENG and the RF receiver. Generated charges from the S-TENG were stored in a capacitor though a rectifier circuit and the charged capacitor was used as a direct power source to operate the wireless temperature sensor. Next, the temperature data was collected using the RF receiver in real time and the temperature information was displayed on a monitor through a simple interface. Fig. 8b shows the charging and discharging sequence when the capacitor is connected to the wireless sensor node. The S-TENG was operated at a rotation speed of 500 rpm for about 3 h to charge a 3 mF capacitor and the energy stored in the capacitor was then used to power the wireless sensor for about 25 s. The capacitor voltage immediately dropped to about 2.5 V as the sensor node was initialized for the operation. The wireless temperature sensor consists of a microcontroller (MSP430F2274) and a 2.4-GHz wireless transceiver (CS2500). The minimum current is about 11 mA and the voltage range is from 1.8 V to 3.6 V, which are required for successfully transmitting data. When the receiver was connected with the computer, the obtained data was transmitted from the wireless sensor to the receiver, and the temperature information was displayed on the computer screen as shown in Fig. 8c. Based on preliminary experiment, it is expected that the proposed S-TENG can realize more potential applications in wireless sensor monitoring networks.

4. Conclusions

In summary, we successfully developed a seesaw-structured triboelectric nanogenerator for converting rotational mechanical energy into electricity. The seesaw system quadrupled the triboelectric contact area and generated double the frequency of electrical output of conventional systems at every rotation cycle. The steady and high-performance electrical output of the S-TENG was achieved in wide ranges of rotation speed and magnetic field strength. The maximum output power density of 13.86 W/m^2 (V_{oc} of 260 V and I_{sc} of 64 μA) was achieved at a rotation speed of 200 rpm under a constant magnetic field strength of 0.2 T. The S-TENG performed as a direct power source to alternately illuminate 120 LEDs in real time and to charge a capacitor with up to 14.2 V in 240 s. With the employed magnetic-coupling contact mechanism, the polymer morphology abrasion was greatly improved compared to that of a sliding mechanism and largely enhanced the reliability and durability of the TENG for scavenging energy from rotational motion. The proposed S-TENG is expected to realize more potential applications such as self-powered wireless sensor nodes in structural health and condition monitoring system.

Acknowledgments

This study was supported by the National Research Foundation of Korea (NRF) grant funded by the Korea government (MSIP) (No.2015R1A4A1041746).

Appendix A. Supplementary data

Supplementary data associated with this article can be found, in the online version, at http://dx.doi.org/10.1016/j.sna.2017.07.021.

References

[1] K. Sohraby, D. Minoli, T. Znati, Wireless sensor networks: technology, protocols, and applications, in: Introduction and Overview of Wireless Sensor Networks, A John Wiley & Sons, Inc., Hoboken, NJ, USA, 2007, pp. 1–31.
[2] I.F. Akyildiz, W. Su, Y. Sankarasubramaniam, E. Cayirci, Wireless sensor networks: a survey, Comput. Networks 38 (2002) 393–422.
[3] H. Messer, A. Zinevich, P. Alpert, Environmental monitoring by wireless communication networks, Science 312 (2006) 713.
[4] P. Constantinou, P.H. Mellor, P.D. Wilcox, A magnetically sprung generator for energy harvesting applications, IEEE/ASME Trans. Mechatron. 17 (2012) 415–424.
[5] S. Roundy, Energy Harvesting for Tire Pressure Monitoring Systems: Design Considerations Proceedings of Power MEMS + MicroMEMS, 2008, pp. 1–6, Sendai, Japan.
[6] M.S. Dresselhaus, I.L. Thomas, Alternative energy technologies, Nature 414 (2001) 332–337.
[7] B. Oregan, M. Gratzel, A low-cost, high-efficiency solar-cell based on dye-sensitized colloidal TiO_2 films, Nature 353 (1991) 737–740.
[8] P.D. Mitcheson, E.M. Yeatman, G.K. Rao, A.S. Holmes, T.C. Green, Energy harvesting from human and machine motion for wireless electronic devices, Proc. IEEE 96 (2008) 1456–1486.
[9] P. Pit, M.Y. Eric, S.H. Andrew, A piezoelectric frequency up-converting energy harvester with rotating proof mass for human body applications, Sens. Actuators A: Phys. 206 (2014) 178–185.
[10] P. Janphuang, R.A. Lockhart, D. Isarakorn, S. Henein, D. Briand, N.F. de Rooij, Harvesting energy from a rotating gear using an AFM-Like MEMS piezoelectric frequency up-converting energy harvester, J. Microelectromech. Syst. 24 (2015) 742–754.
[11] X. Wu, M. Parmar, D.W. Lee, A seesaw structured energy harvester with Superwide bandwidth for TPMS application, IEEE/ASME Trans. Mechatron. 5 (19) (2014) 1514–1522.
[12] J.H. Park, T.W. Lee, S.D. Kim, S.H. Park, Design and experimental verification of flexible plate-type piezoelectric vibrator for energy harvesting system, Int. J. Precis. Eng. Manuf.-Green Technol. 3 (2016) 253–259.
[13] C.B. Williams, C. Shearwood, M.A. Harradine, P.H. Mellor, T.S. Birch, R.B. Yates, Development of an electromagnetic microgenerator, IEE Proc.-Circuits Devices Syst. 148 (2011) 337–342.

[14] S.P. Beeby, R.N. Torah, M.J. Tudor, P. Glynne-Jones, T. O'Donnell, C.R. Saha, S. Roy, A micro electromagnetic generator for vibration energy harvesting, J. Micromech Microeng 17 (7) (2007) 1257–1265.
[15] H.C. Park, J.H. Kim, Electromagnetic induction energy harvester for high-speed railroad applications, Int. J. Precis. Eng. Manuf.-Green Technol. 3 (1) (2016) 41–48.
[16] M. El-hami, P. Glynne-Jones, N. MWhite, M. Hill, S. Beeby, E. James, A.D. Brown, J.N. Ross, Design and fabrication of a new vibration-based electromechanical power generator, Sens. Actuators A: Phys. 92 (1–3) (2001) 335–342.
[17] Y. Naruse, N. Matsubar, K. Mabuchi, M. Izumi, S. Suzuki, Electrostatic micro power generation from low-frequency vibration such as human motion, J. Micromech. Microeng. 19 (9) (2009) 094002.
[18] P.D. Mitcheson, P. Miao, B.H. Stark, E.M. Yeatman, A.S. Holmes, T.C. Green, MEMS electrostatic micropower generator for low frequency operation, Sens. Actuators A: Phys. 115 (2–3) (2004) 23–529.
[19] S.H. Wang, L. Lin, Z.L. Wang, Triboelectric nanogenerators as self-powered active sensors, Nano Energy 11 (2015) 436–462.
[20] G. Zhu, B. Peng, J. Chen, Q.S. Jing, Z.L. Wang, Triboelectric nanogenerators as a new energy technology: from fundamentals, devices, to applications, Nano Energy 14 (2015) 126–138.
[21] Y. Yang, H. Zhang, S. Lee, D. Kim, W. Hwang, Z.L. Wang, Hybrid energy cell for degradation of methyl orange by self-powered electrocatalytic oxidation, Nano Lett. 13 (2) (2013) 803–808.
[22] F.R. Fan, Z.Q. Tian, Z.L. Wang, Flexible triboelectric generator, Nano Energy 1 (2012) 328–334.
[23] F.R. Fan, L. Lin, G. Zhu, W. Wu, R. Zhang, Z.L. Wang, Transparent triboelectric nanogenerators and self-powered pressure sensors based on micropatterned plastic films, Nano Lett. 12 (6) (2012) 3109–3114.
[24] P. Bai, G. Zhu, J. Chen, Q.S. Jing, W.Q. Yang, J.S. Ma, G. Zhang, Z.L. Wang, Cylindrical rotating triboelectric nanogenerator, ACS Nano 7 (7) (2013) 6361–6366.
[25] L. Lin, S.H. Wang, Y.N. Xie, Q.S. Jing, Y.F. Niu, Z.L. Wang, Segmentally structured disk triboelectric nanogenerator for harvesting rotational mechanical energy, Nano Lett. 13 (6) (2013) 2916–2923.
[26] H.L. Zhang, X.D. Zhong, Y.J. Su, Y.S. Zhou, C.G. Hu, Z.L. Wang, Single-Electrode-Based rotating triboelectric nanogenerator for harvesting energy from tires, ACS Nano 8 (1) (2014) 680–689.
[27] Y.F. Lia, G. Cheng, Z.H. Lin, J. Yang, L. Lin, Z.L. Wang, Single-electrode-based rotationary triboelectric nanogenerator and its applications as self-powered contact area and eccentric angle sensors, Nano Energy 11 (2015) 323–332.
[28] H.Y. Guo, J. Chen, M.H. Yeh, X. Fan, Z. Wen, Z.L. Li, C.G. Hu, Z.L. Wang, An ultrarobust high-performance triboelectric nanogenerator based on charge replenishment, ACS Nano 9 (5) (2015) 5577–5584.
[29] Y.K. Shuang, J. Chen, X.B. Cheng, Z. Guang, Z.L. Wang, Two dimensional rotary triboelectric nanogenerator as a portable and wearable power source for electronics, Nano Energy 17 (2015) 10–16.
[30] S.W. Cheng, C.Z. Gao, W. Tang, H.R. Zhu, Y. Han, Q.W. Jiang, T. Li, X. Cao, Z.L. Wang, Self-powered cleaning of air pollution by wind driven triboelectric nanogenerator, Nano Energy 14 (2015) 217–225.
[31] L.B. Huang, G.X. Bai, M.C. Wong, Z.B. Yang, W. Xu, J.H. Hao, Magnetic-assisted noncontact triboelectric nanogenerator converting mechanical energy into electricity and light emissions, Adv. Mater. 28 (14) (2016) 2744–2751.
[32] J. Lowell, A.C. Rose-Innes, Contact electrification, Adv. Phys. 29 (6) (1980) 947–1023.
[33] G. Zhu, C.F. Pan, W.X. Guo, C.Y. Chen, Y.S. Zhou, R.M. Yu, Z.L. Wang, Triboelectric-Generator-Driven pulse electrodeposition for Micropatterning, Nano Lett. 12 (9) (2012) 4960–4965.
[34] Q.S. Jing, Y.N. Xie, G. Zhu, R.P.S. Han, Z.L. Wang, Self-powered thin-film motion vector sensor, Nat. Commun. 6 (2015) 8031.
[35] X.N. Wen, Y.J. Su, Y. Yang, H.L. Zhang, Z.L. Wang, Applicability of triboelectric generator over a wide range of temperature, Nano Energy 4 (2014) 150–156.
[36] Y. Zhang, H.Y. Keum, K.D. Park, R. Bashir, S. Kim, Micro-Masonry of MEMS sensors and actuators, J. Micromech. Microeng 23 (2) (2014) 094002.
[37] A. Choi, J.Y. Kim, J.E. Lee, H. Jung, Effects of PDMS curing ratio and 3D micro-pyramid structure on the formation of an in vitro neural network, Curr. Appl. Phys. 9 (2009) 308–314.
[38] Z.L. Wang, Triboelectric nanogenerators as new energy technology for self-powered systems and as active mechanical and chemical sensors, ACS Nano 7 (11) (2013) 9533–9557.
[39] Y. Wu, Q.S. Jing, J. Chen, P. Bai, J.J. Bai, G. Zhu, Y.J. Su, Z.L. Wang, A self-powered angle measurement sensor based on triboelectric nanogenerator, Adv. Funct. Mater. 25 (14) (2015) 2166–2174.
[40] Y. Yang, H.L. Zhang, Z.H. Lin, Y.S. Zhou, Q.S. Jing, Y.J. Su, J. Yang, J. Chen, Z.L. Wang, Human skin based triboelectric nanogenerator for harvesting biomechanical energy and as self-powered active tactile sensor system, ACS Nano 7 (10) (2013) 9213–9222.
[41] S.M. Niu, Z.L. Wang, Theoretical systems of triboelectric nanogenerator, Nano Energy 14 (2015) 161–192.
[42] S.M. Niu, S.H. Wang, L. Lin, Y. Liu, Y.S. Zhou, Y.F. Hua, Z.L. Wang, Theoretical study of contact-mode triboelectric nanogenerators as an effective power source, Energy Environ. Sci. 6 (2013) 3576–3583.
[43] D.J. Jang, Y.H. Kim, T.Y. Kim, K.S. Koh, U.Y. Jeong, J.H. Choa, Force-assembled triboelectric nanogenerator with high-humidity-resistant electricity generation using hierarchical surface morphology, Nano Energy 20 (2016) 229–283.
[44] Q. Leng, H.Y. Guo, X.M. He, G.L. Liu, Y. Kang, C.G. Hu, Y. Xi, Flexible interdigital-electrodes-based triboelectric generators for harvesting sliding and rotating mechanical energy, J. Mater. Chem. A 2 (2014) 19427–19434.
[45] X.N. Wen, W.Q. Yang, Q.S. Jing, Z.L. Wang, Harvesting broadband kinetic impact energy from mechanical triggering/vibration and water waves, ACS Nano 7 (8) (2014) 7405–7412.
[46] L. Lin, Y. Xie, S. Niu, S. Wang, P.K. Yang, Z.L. Wang, Robust triboelectric nanogenerator based on rolling electrification and electrostatic induction at an instantaneous energy conversion efficiency of ~ 55%, ACS Nano 1 (9) (2014) 922–930.
[47] G. Zhu, J. Chen, T.J. Zhang, Q.S. Jing, Z.L. Wang, Radial-arrayed rotary electrification for high performance triboelectric generator, Nat. Commun. 5 (2014) 3426.

Biographies

Jingui Qian received the B.Eng. degree in mechanical engineering from Wenzhou University, China in 2015. He is currently working toward the M.Eng. degree in mechanical engineering in MEMS and Nanotechnology Laboratory, Department of Mechanical Engineering, Chonnam National University, Korea. His current research interests include PowerMEMS and nanogenerator, energy harvesting and energy storage, polymer material, self-powered sensor.

Xuan Wu received the B.Eng. and M.Eng. degrees in mechanical engineering from Chongqing University of Technology, China, in 2009 and 2012. And he received the Ph.D. degree in mechanical engineering in MEMS and Nanotechnology Laboratory at Chonnam National University, South Korea. His research was rewarded as Best Paper Awards in the 5th Japan-China-Korea MEMS/NEMS International Conference and 2013 Kroean Society for Precision Engineering Conference. He was also rewarded as Outstanding Self-Financed Students Abroad by Chinese Government in 2015. Currently, he is the Professor of Mechanical Engineering at JiangSu University in China. His research interests include energy-harvesting technology, MEMS device design and fabrication, flexible and wearable electronics, and graphene local anodic lithography technology.

Dong-Su Kim received his BS degree in electronics engineering from Chosun University, Korea in 2013 and MS in mechanical engineering from Chonnam National University, Korea in 2016. Currently he is pursuing his doctoral degree in mechanical engineering at MEMS and Nanotechnology Laboratory, Department of Mechanical Engineering, Chonnam National University, Korea. His research activity is primarily focused on design and fabrication new class of Bio-MEMS device for drug screening applications.

Dong-Weon Lee received the Ph.D. degrees in Mechatronics engineering from Tohoku University, Sendai, Japan, in 2001. He has been a Professor of Mechanical Systems Engineering at Chonnam National University (CNU), Republic of Korea since March of 2004. Previously, he was with the IBM Zurich Research Laboratory in Switzerland, working mainly on micro cantilever devices for chemical AFM applications. At CNU, his research interests include smart cantilever devices, miniaturized energy harvester, smart materials and structures, and nanoscale transducers. He is a member of the technical program committee of IEEE Sensors Conference, Transducers, and Micro processes and Nanotechnology Conference (MNC).